

This document is confidential and is proprietary to the American Chemical Society and its authors. Do not copy or disclose without written permission. If you have received this item in error, notify the sender and delete all copies.

Semiconductor-to-Metal Transition in Rutile TiO₂ Induced by Tensile Strain

Journal:	<i>Chemistry of Materials</i>
Manuscript ID	cm-2016-04881e
Manuscript Type:	Article
Date Submitted by the Author:	16-Nov-2016
Complete List of Authors:	Benson, Eric; National Renewable Energy Laboratory, Miller, Elisa; National Renewable Energy Laboratory, Nanayakkara, Sanjini; National Renewable Energy Laboratory, Chemical and Material Science Division Svedruzic, Drazenka; NREL, Biosciences Ferrere, Suzanne; National Renewable Energy Laboratory, Basic Sciences Neale, Nathan; National Renewable Energy Laboratory, van de Lagemaat, Jao; National Renewable Energy Laboratory, Gregg, Brian; NREL, Basic Sciences

SCHOLARONE™
Manuscripts

Semiconductor-to-Metal Transition in Rutile TiO₂ Induced by Tensile Strain

Eric E. Benson[‡], Elisa M. Miller, Sanjini U. Nanayakkara, Drazenka Svedruzic, Suzanne Ferrere, Nathan R. Neale, Jao van de Lagemaat, and Brian A. Gregg.

National Renewable Energy Laboratory, 15013 Denver West Parkway, Golden, Colorado 80401, United States

Abstract

We report the first observation of a reversible semiconductor-to-metal transition in titanium dioxide. Application of tensile strain to a ~50 nm film of rutile TiO₂ thermally grown on a superelastic nitinol (NiTi intermetallic) substrate causes reversible degenerate doping as evidenced by electrochemistry, X-ray photoelectron spectroscopy (XPS), and conducting atomic force microscopy (CAFM). Cyclic voltammetry and impedance measurements show behavior characteristic of a highly doped n-type semiconductor for unstrained TiO₂ transitioning to metallic behavior under tensile strain. The transition reverses when strain is removed. Valence band XPS spectra show that samples strained to 5% exhibit metallic-like intensity near the Fermi level. Strain also induces a distinct transition in CAFM current-voltage curves from rectifying (typical of an n-type semiconductor) to ohmic (metal-like) behavior. We propose that strain raises the energy distribution of oxygen vacancies (n-type dopants) near the conduction band and causes an increase in carrier concentration. As the carrier concentration is increased, the width of the depletion region is reduced, which then permits electron tunneling through the space charge barrier resulting in the observed metallic behavior.

Introduction

The ability to dynamically tune the electronic properties of a single material with strain has opened a new and rapidly expanding area of research. Traditionally, a material possesses a

single set of static properties (electrochemical, photophysical, *etc.*) that are derived from its atomic structure, *i.e.*, coordination number, symmetry, bond lengths, and bond angles. However, physical deformation through mechanical stress can alter the local atomic environment allowing for novel properties to emerge.¹ This principle appears in biological systems wherein static and dynamic mechanical forces within enzymes are thought to play an essential role in catalysis (entatic state hypothesis).²⁻⁴ Similarly, in engineered materials, the chemical reactivity and electrocatalytic properties have been shown to be sensitive to mechanical strain.⁵⁻¹⁰ The fundamental electronic properties of semiconductors have been theoretically shown to be altered through static strain by exploiting lattice mismatch¹¹ as well as dynamically by using flexible nano-scale architectures.¹² The resulting strain has been experimentally shown to alter a material's bandgap,¹³ influence carrier mobility,¹⁴ and effect indirect to direct optical transitions.^{15, 16} In addition, we have demonstrated that tensile strain of a NiOOH-coated stainless steel metal electrode leads to reversible increases in the rates of electron transfer to a redox couple in solution, charge transport through a surface film, and electrocatalysis.⁷

Our team and others have been exploring metal oxide semiconductors as light-harvesting photoelectrodes¹⁷⁻²³ as well as protective layers on photovoltaic semiconductors²⁴⁻²⁷ for water photoelectrolysis. Since the photophysical and catalytic properties of TiO₂ are well known, it offers an excellent platform to study strain-induced effects, specifically whether or not strain can be used to engineer the (photo)catalytic properties of these oxide semiconductors. Previous theoretical treatments have suggested that 5% biaxial compressive strain of an anatase TiO₂ crystallite can cause a 5-fold increase in the area percentage of the more catalytically active (001) surface.²⁸ Similarly, Wei and coworkers theoretically showed that the bandgap of rutile and anatase can be altered using uniaxial, hydrostatic, and epitaxial strain.²⁹ First-principle

calculations³⁰ show that the application of external strain changes the relative formation energies of the different types of oxygen vacancies (OVs) (the major n-type dopant in TiO₂).³¹ Under some circumstances, OVs are calculated to aggregate into structures that are similar to the conducting suboxides that exhibit metallic behavior.³²

Semiconductor-to-metal (S-M) transitions under tensile strain also have been calculated for a number of materials such as Si³³ and semiconducting transition metal dichalcogenides.^{34, 35} Recent experimental results are confirming these S-M transitions. For example, Song *et al.* demonstrated that applying a tensile strain to MoTe₂³⁶ affects a phase change from 2H to 1T', resulting in a reversible S-M transition localized under the AFM tip that applied the strain. Misfit-strained VO₂³⁷ and OV-strained VO₂³⁸ both exhibit thermally activated S-M transitions, albeit with significant hysteresis that makes these only quasi-reversible. In contrast to these reports, we show that tensile strain results in a fully reversible S-M transition in bulk thin films of rutile TiO₂ grown on a superelastic intermetallic nitinol (NiTi) substrate. This is confirmed via electrochemistry, X-ray photoelectron spectroscopy (XPS), and conducting atomic force microscopy (CAFM). Similar to previous reports, the mobility and formation energy of OVs are attributed to this transition. This is a promising result for improving the (photo)catalytic properties of metal oxides.

Results and Discussion

As a pseudo-superelastic metal, the intermetallic NiTi offers up to ~8% elastic deformation arising from a solid-state lattice transition.³⁹ Previously Bard *et al.* have shown that by depositing Pt on a NiTi substrate and utilizing the shape memory properties of NiTi, tensile and compressive strain could modulate the oxygen reduction reaction.⁸ Due to the oxophilic

nature of titanium, calcination at elevated temperatures results in the formation of a capping TiO_2 film. Our initial efforts are focused on 50 nm and 100 nm rutile TiO_2 films that were grown by aerobic oxidation at 500 $^\circ\text{C}$ for 30 and 120 min, respectively.^{40–42}

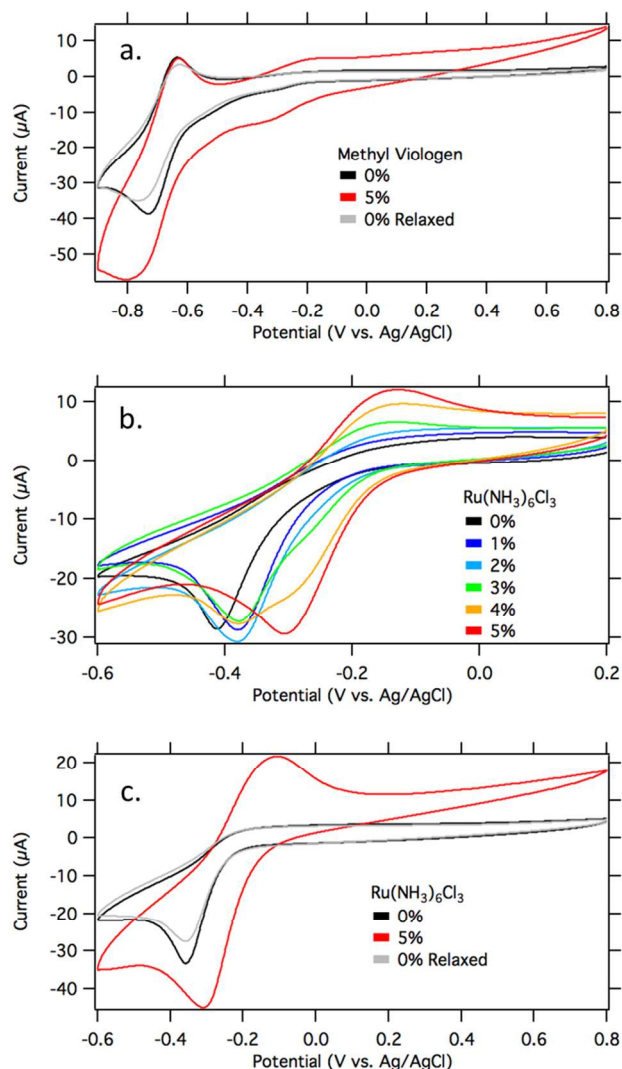


Figure 1. a) Cyclic voltammograms (CVs) of 1 mM methyl viologen at 0%, 5%, and relaxed to 0% strain of a 50 nm TiO_2 film. b) 1 mM ruthenium hexamine at 0% – 5% applied external strain at 1% strain intervals c) CVs of 1 mM ruthenium hexamine in at 0%, 5%, and relaxed back to 0% external strain. All scans were taken in 0.1 M phosphate buffer (pH 7) on a 50 nm TiO_2 film at 50 mV/s with Ag/AgCl reference and Pt counter electrodes.

Electrochemistry. Our initial experiments probed the current-voltage response of these 50 nm rutile TiO_2 films under tensile strain using methyl viologen (MV) as a simple redox mediator.

The cyclic voltammogram (CV) on the unstrained sample shows a mostly reversible one-electron couple at -0.68 V, with a peak-to-peak splitting of 94 mV (Figure 1a, black trace). The observed splitting of the MV couple from the ideal 57 mV may be attributed to slow electron transfer kinetics of the TiO₂ films.⁴³ Under 5% tensile strain, the electrochemical behavior of the MV couple remains reversible with a small increase in background current (Figure 1a, red trace). Relieving the stress allows the TiO₂ to return to its original state, with a corresponding CV curve nearly identical to the original unstrained response (Figure 1a, grey trace). Since the redox couple potential is cathodic of the surface state potential (-0.40 V, *vide infra*), we expect the TiO₂ to be able to donate and receive electrons from MV in solution.

We next investigated the current-voltage response using the ruthenium hexamine redox couple similar to our prior report on NiOOH/stainless steel.⁷ Here, the CV curve is quite different than with the MV couple. In the TiO₂ unstrained state (Figure 1b, black curve), the ruthenium hexamine reduction is completely irreversible with a peak current $I_p = -0.41$ V for the Ru³⁺ reduction. This irreversible behavior is expected for an n-type semiconductor with a surface state (SS) potential that is not well-matched (anodic) to the Ru²⁺ oxidation potential (Figure S3).⁴⁴

Also in contrast to the MV reduction, systematically increasing the tensile strain from 0% to 5% shifts the ruthenium hexamine reduction potential anodically to $I_p = -0.30$ V (Figure 1b, red curve). Critically, strain also induces the re-oxidation wave to become apparent, with the 5% strain CV response (Figure 1b, red curve) resembling that of a (metallic) gold electrode (Figure S3) with a half-wave potential of -0.21 V and 180 mV of splitting. When allowed to relax to its original unstrained state (Figure 1c, grey curve), the reduction potential shifts cathodically, back to its previous unstrained, irreversible state with a complete loss of the re-oxidation wave. The

1
2
3 presence of the re-oxidation wave suggests that the nature of the film has changed substantially,
4
5 enabling the TiO_2 to accept electrons at a potential that should be in its bandgap. We hypothesize
6
7 that the observed electrocatalytic properties are due to a strain-induced, semiconductor-to-metal
8
9 transition (S-M) within the TiO_2 film.
10
11

12
13 An alternative explanation for this behavior is that fissuring (cracking) of the film surface
14
15 results in exposure of the metallic substrate. To eliminate this possibility, a sample was strained
16
17 beyond its elastic limit to intentionally crack the TiO_2 film. Figure 2a shows a scanning electron
18
19 microscope (SEM) image of the fissures generated by straining from 0% to 7% for 100 cycles
20
21 and then held at 7% strain for 12 h. The CVs of the TiO_2 is similar both before straining and after
22
23 cracking (Figure 2b). After 7% strain is applied, an increase in the charging current as well as an
24
25 increase in peak current is observed, consistent with an increase in electroactive surface area.
26
27 However, the shift in reduction potential and presence of the oxidative wave, observed when the
28
29 film was strained reversibly, were not observed for the intentionally cracked film. SEM images
30
31 taken of the polished samples, after oxidation at 500 °C, and at 5% strain show no change in the
32
33 surface morphology (Figure S5). We conclude that surface fissuring and exposure of active
34
35 sites/metallic substrate is not responsible for the strain-induced changes observed in <5%
36
37 strained films (shown in Figure 1).
38
39
40
41
42
43
44
45
46
47
48
49
50
51
52
53
54
55
56
57
58
59
60

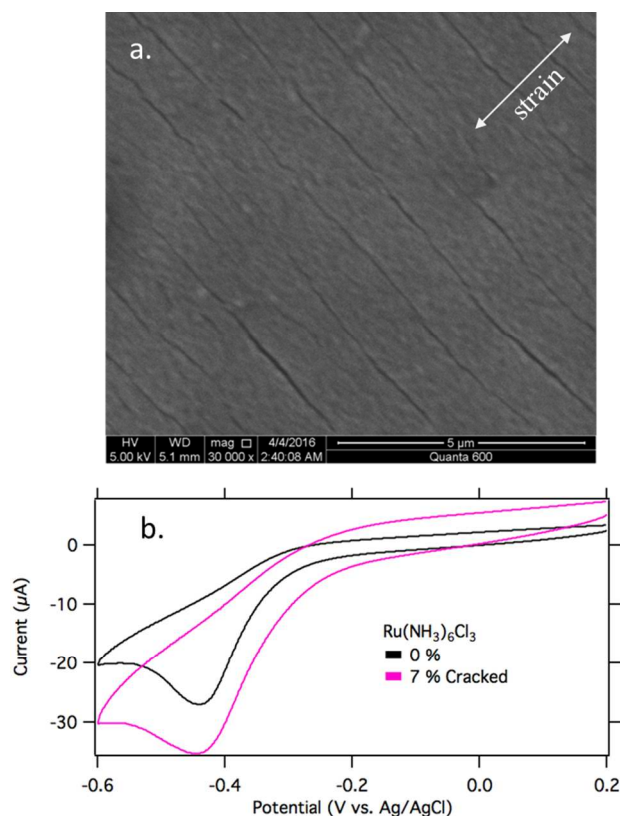


Figure 2. a) SEM image of the cracked TiO₂ film under 7% strain showing the formation of fissures forming perpendicular to the direction of strain. b) CVs of 1 mM ruthenium hexamine at a intentionally cracked 50 nm TiO₂ film at 0% and 7% external applied strain

Electrochemical impedance spectroscopy (EIS) was utilized to further characterize the properties of the TiO₂ film. Figure 3a shows the Nyquist plot and circuit model used to fit the data of relaxed and strained samples. The plot shows two RC time constants, one that is independent of strain and another that shows a strong dependence with tensile strain. The circuit was modeled as a modified Randles circuit with an additional resistance (R_c) and capacitance (C_c) in series, representing an additional chemical capacitance due to adsorption of the phosphate electrolyte on the surface of TiO₂.⁴⁵ This is a reasonable model since this additional RC time constant is not observed in 0.5 M H₂SO₄ or 1 M NaOH solutions. While the solution resistance (R_s) and chemical capacitance (C_c , R_c) do not change appreciably with strain, the polarization resistance (R_p) is lowered by a factor of four, from 15.0 kΩ to 3.6 kΩ, for unstrained and 5%

strain, respectively (Table S1). Furthermore the phase angle of the constant phase element is depressed by 4° as the sample is strained to 5%. These factors lead to an increase in the effective capacitance from $6.5 \mu\text{F}/\text{cm}^2$ to $14.9 \mu\text{F}/\text{cm}^2$ and reflects a broader distribution and increase in SS observed in the Mott-Schottky plots described below.⁴⁶ Similar to the CV curves, once the external strain is removed and the sample is allowed to relax, these values return to their pre-strained state.

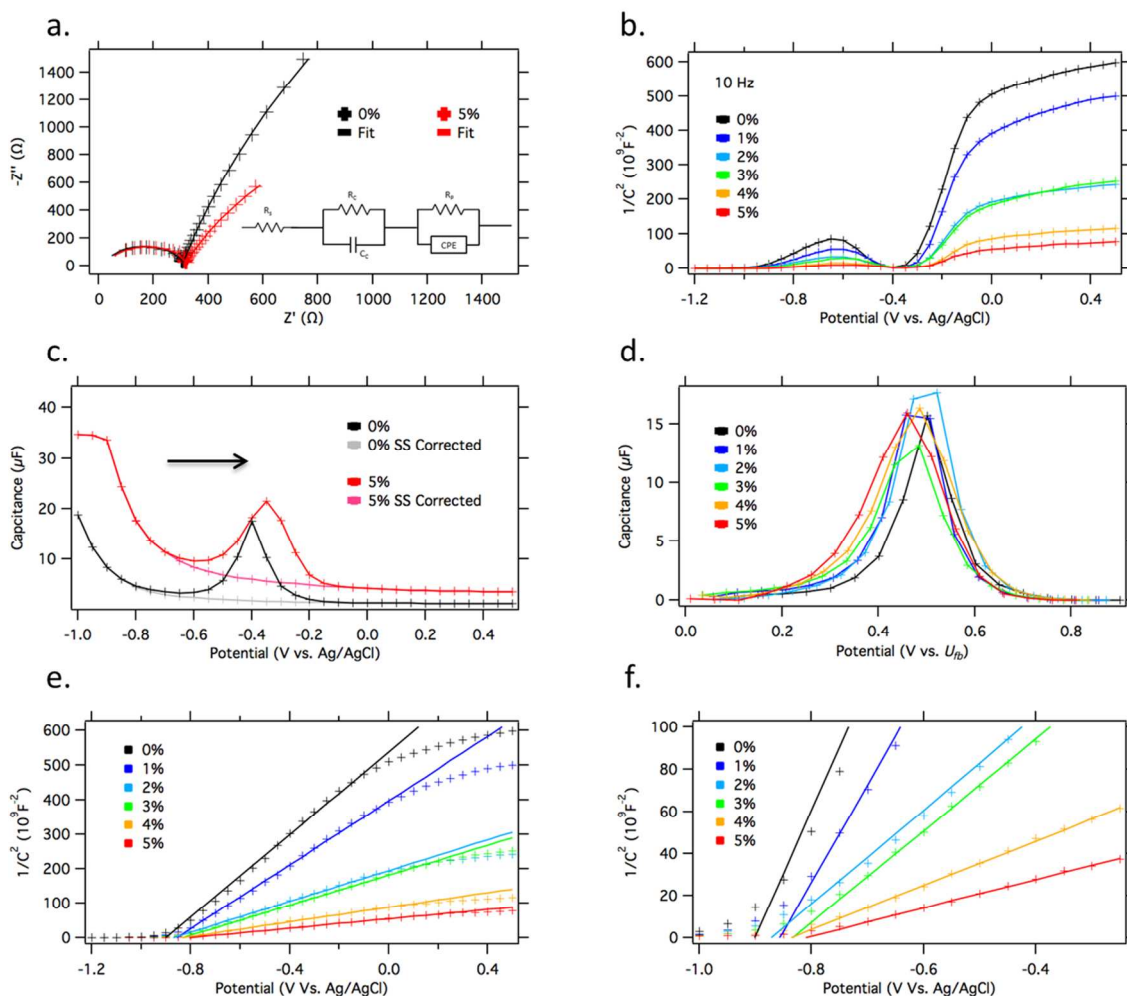


Figure 3. a) Nyquist plot and circuit model for 50 nm TiO_2 films (0 and 5% strain) in 1 mM ruthenium hexamine in 0.1 M phosphate buffer taken at 0.00 V where no redox processes take place. Data is taken from 100 Hz to 2 MHz. b) Mott-Schottky (MS) plot of strained TiO_2 films taken at 10 Hz c) Series capacitance of 0% and 5% strain before and after ("corrected") surface state (SS) deconvolution d) SS capacitance plotted vs. U_{fb} used for deconvolution of MS plot e) SS deconvoluted MS plot and fits (solid lines) and f) expanded region of the MS plot near the U_{fb}

Mott-Schottky (MS) analysis of the voltage-dependent EIS data taken at 10, 100, and 1000 Hz was performed to approximate the flat-band potential (U_{fb}) and donor density (N_d) of the rutile TiO_2 films according to Equation 1:

$$C^{-2} = \frac{2(U - U_{fb} - kT/e)}{e\epsilon_0\epsilon N_d A^2} \quad (1)$$

where C is the capacitance, U the applied potential, k is the Boltzmann constant, T is the temperature, e is the electron charge, ϵ_0 is the permittivity of vacuum, ϵ is the dielectric constant of rutile TiO_2 ($\epsilon = 173$),⁴⁷ and A is the surface area. At lower frequencies (10 Hz), the presence of SS is observed in the MS and series capacitance vs. voltage plots (Figure 3b and 3c, respectively). At higher frequencies (100 and 1000 Hz), the contribution from SS is washed out by slow kinetics (Figure S6).

The presence of such a large number of SS, presumably OVs,³¹ prevents quantitative analysis of the MS plots.^{32, 37} Therefore, we deconvoluted the SS capacitance from the semiconductor capacitance at 10 Hz as shown in Figure 3c. This procedure provides reasonable MS plots (Figure 3e), albeit with non-physical absolute values of N_d (Table 1; calculated from the MS plot slopes) likely resulting from nonuniformities in thickness and doping across the film. Nevertheless, the trends in N_d and U_{fb} are reasonable and reproducible, regardless of frequency and any correction of SS effects (Figure S6). The apparent carrier density increases by about a factor of 10 upon 5% strain, and U_{fb} shifts anodically by 91 mV, consistent with the CV results (Table 1). These changes could be interpreted as stemming from new OVs created by

strain, but we consider this explanation unlikely since it would require the reversible formation and destruction of $\sim 10^{22}$ dopants/cm³ coupled with oxygen diffusion into and out of the film. Rather, it seems more likely that the existing bulk OV distribution is shifted higher in energy with strain, analogous to the SS distribution described below. As the carrier concentration increases with strain, the associated depletion width, W , decreases according to Equation 2.

$$W \approx \sqrt{\frac{2\epsilon_0\epsilon U}{qN_d}} \quad (2)$$

Taking values obtained from the MS plots, we get an approximate depletion width of 11 nm for the unstrained sample with a bias of 100 mV. Upon 5% tensile strain, this is reduced to 3.5 nm, which is in the range where appreciable electron tunneling can take place.^{43, 48} A proposed band diagram can be found in Figure 4a.

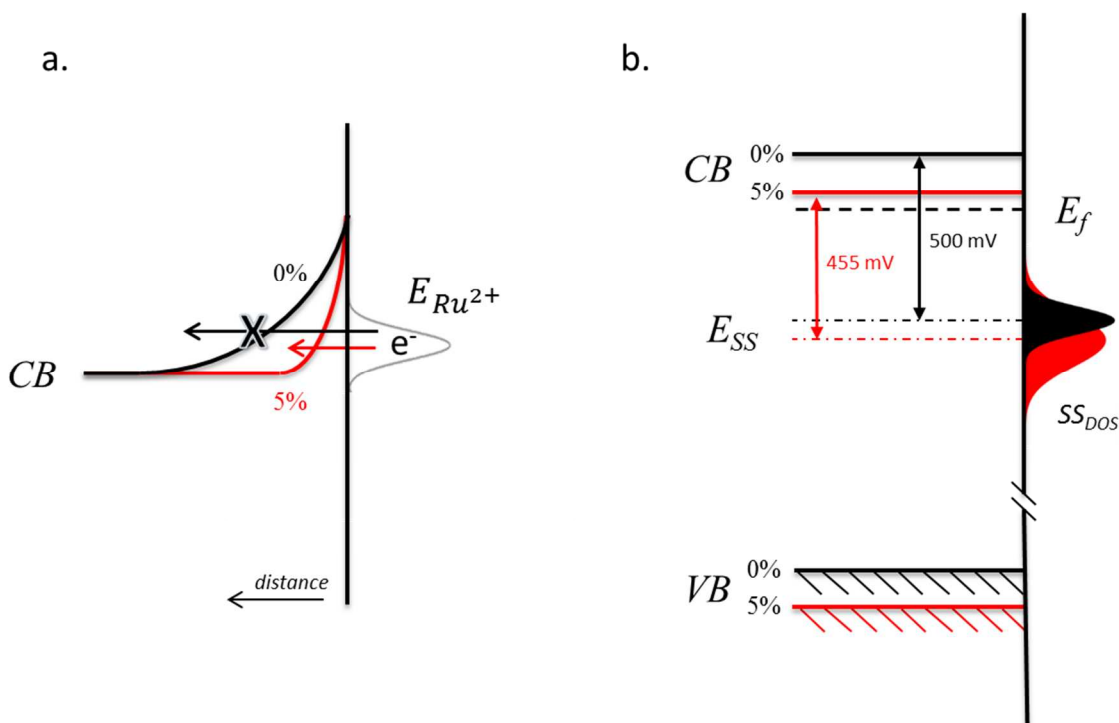


Figure 4. a) Proposed band diagram showing the effect of strain on the depletion width and resulting electron tunneling from the reduced species to the conduction band and b) energy diagram under flat band conditions showing the effect of strain on the surface state energy level distribution and the shift of the conduction band relative to the Fermi level, E_f .

Finally, the approximately Gaussian SS distribution also shifts anodically with strain, but to a lesser degree (up to 46 mV under 5% strain, Figure 3c). Overall, strain increases the integrated capacitance (*i.e.*, the SS density) by 46%, both broadening the SS distribution and shifting the SS peak 45 mV closer to the conduction band (Figure 3d). We surmise that these cooperative effects result in the observed S-M transition.

Table 1. Donor density, flatband potentials, integrated surface state capacitance, and surface state peak potential of strained TiO₂ derived from MS plots taken at 10 Hz.

Strain	$N_d(\text{cm}^{-3})$	U_{fb} (V vs. Ag/AgCl)	SS Capacitance (F)	SS Potential (V vs. U_{fb})
0%	$1.71 \cdot 10^{21}$	-0.901	$2.66 \cdot 10^{-6}$	0.500
1%	$2.20 \cdot 10^{21}$	-0.857	$2.95 \cdot 10^{-6}$	0.479
2%	$4.56 \cdot 10^{21}$	-0.872	$3.80 \cdot 10^{-6}$	0.496
3%	$4.69 \cdot 10^{21}$	-0.834	$2.90 \cdot 10^{-6}$	0.464
4%	$9.67 \cdot 10^{21}$	-0.836	$4.02 \cdot 10^{-6}$	0.478
5%	$1.51 \cdot 10^{22}$	-0.810	$3.88 \cdot 10^{-6}$	0.455
0% Relaxed	$2.91 \cdot 10^{21}$	-0.880	$3.97 \cdot 10^{-6}$	0.474

The majority of carriers, then, must derive from bulk dopants (sub-surface "dry" oxygen vacancies) rather than the surface states (hydrated OV_s, *i.e.*, pairs of OH groups)⁴⁹ that we observe in capacitance measurements. The two populations of OV_s are expected to be in dynamic equilibrium since OV_s are known to be mobile.⁵⁰ This equilibrium implies that the observed increase in SS density with strain indicates a greater relative increase in energy of the bulk OV_s, thus driving additional OV_s to the surface. For example, Li *et al.*⁴⁹ observed that dry

OVs diffuse away from strained regions in a (110) TiO_2 surface (produced by introducing subsurface clusters of argon ions); this demonstrates that strained OVs are at a higher energy than unstrained OVs. Since our entire ~ 50 nm thick polycrystalline film is affected by strain, it is reasonable to assume sub-surface OVs are at a higher energy level distribution than those in unstrained samples thus moving the Fermi level closer to the conduction band.

X-Ray Photoelectron Spectroscopy. In order to further confirm the quasi-metallic nature of the strained films, XPS was performed on 100 nm films at 0% and 5% strain. High-resolution XPS spectra did not show any appreciable changes in the Ti or O environments under tensile strain (Figure S7), and the O:Ti ratio remained constant at 2.5. Within our XPS experimental resolution (± 50 meV), the peak positions and shapes are not changing with strain. Figure 5 shows the XPS (left) and ultraviolet photoelectron spectroscopy (UPS, right) of the valence band region of the TiO_2 film under no strain (black traces) as well as the identical sample under 5% tensile strain (red traces). A small but reproducible photoelectron intensity at the Fermi level ($E_F = 0$ eV) is observed in the XPS spectra of TiO_2 under 5% tensile strain, indicative of a metallic-like density of states. However, in the UPS spectra this is not observed and agrees with the OVs being mobile and equilibrating on the surface, as the top 0 - 3 nm of TiO_2 show similar features regardless of strain. Yet the dry, sub-surface (>3 nm) OVs show metallic-like features arising from the aforementioned shift to higher energy. Although the XPS shows variable, low levels ($<2\%$) of nickel present at the surface (top 10 nm), the electrochemical behavior as well as the observed increase in intensity at the Fermi level was reproducible regardless of the nickel concentration at the surface.

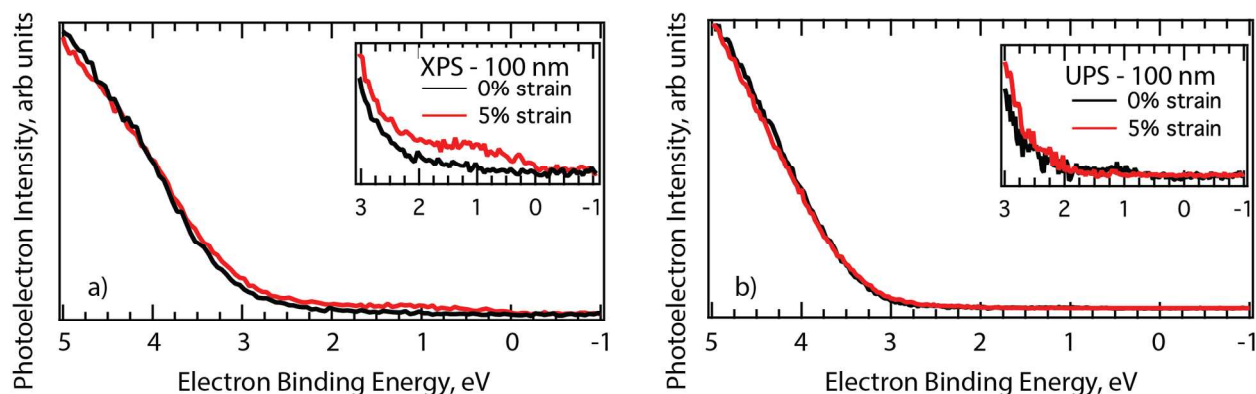


Figure 5. a) XPS and b) UPS valence band region of **TiO₂/NiTi** under 0% (black trace) and 5% (red trace) strain. The photoelectron intensity at $E_F = 0$ eV is present in the XPS and not UPS, which is emphasized in the insets.

Conducting Atomic Force Microscopy. Finally, we used CAFM to probe the proposed S-M transition of the 50 nm TiO₂ films. As shown in Figure 6, no strain (black trace) resulted in insulating/rectifying behavior as expected for an n-type semiconductor with an apparent resistance of ~ 10 G Ω near zero field. When 5% strain is applied (red trace), the sample becomes ohmic (metal-like) in behavior with the resistance dropping to 15.6 M Ω . Once the strain is removed (blue trace), the sample returns to a rectifying junction. This behavior was reproduced over various points on each TiO₂ film and with different nitinol samples. These CAFM results provide additional evidence that strain induces a reversible S-M transition in rutile TiO₂ thin film.

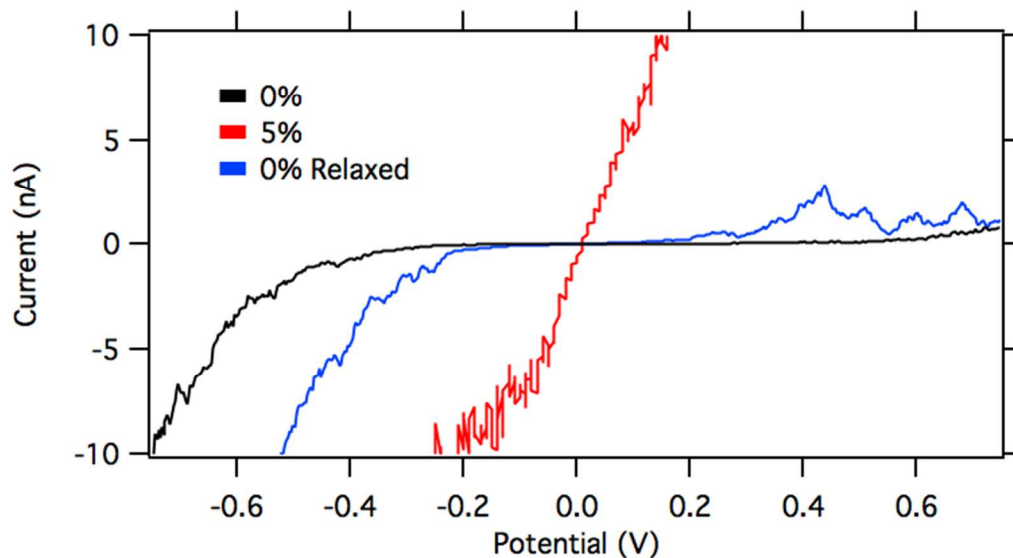


Figure 6. Current-voltage curves obtained from CAFM measurements of 50 nm TiO₂ films at 0%, 5% and then relaxed to 0% strain.

Conclusion

The use of strain to dynamically modify the photophysical and catalytic properties of materials is a burgeoning field. Herein, we report that applying tensile strain to a rutile TiO₂ thin film results in a reversible increase in conductivity, leading to a semiconductor-to-metal transition over the bulk of the TiO₂ thin film. Our experimental results strongly suggest that strain shifts the dopant level (OV) distribution to higher energy, eventually resulting in possible overlap with the conduction band. Additionally with the increase in carrier concentration the depletion width is decreased by a factor of three, which we hypothesize can then lead to electron tunneling from solution into the conduction band. These results highlight the opportunities for the reversible tuning of material properties with applied strain.

Methods

Nitinol (NiTi) Preparation. Superelastic NiTi foil (0.05 mm thickness) was obtained from Alpha Aesar and mechanically polished with emery paper of increasing grit, then finally 1- μm diamond, 0.25- μm diamond, and 0.05- μm alumina polish. After polishing, the samples were sonicated for 10 min in sequential baths of deionized water, ethanol, and isopropanol; then they were dried under a stream of nitrogen. The foils were then oxidized at 500 $^{\circ}\text{C}$ under aerobic conditions for 30 or 120 min. Due to the oxophilic nature of titanium, calcination at elevated temperatures results in a rutile TiO_2 capping layer, wherein the thickness can be controlled by annealing time and temperature.^{40, 41} From UV-Vis interferograms, the thickness of the TiO_2 film is estimated to be ~ 50 and 100 nm for samples oxidized 30 and 120 min, respectively.⁴² All TiO_2 films showed some nickel on the surface by XPS, and its concentration was Nitinol batch dependent. However the varying concentrations did not noticeably affect either the electrochemical or the XPS results.

Characterization. UV-Vis-NIR spectra were collected using a Shimadzu UV-3600 spectrophotometer. XPS and UPS data were obtained on a Physical Electronics 5600 system using Al $\text{K}\alpha$ and He (I) radiation, respectively, which has been described in detail previously.⁵¹ Briefly, the XPS and UPS setups were calibrated with Au metal, which was cleaned via Ar-ion sputtering. The energy uncertainty for XPS and UPS is ± 0.05 eV and ± 0.025 eV, respectively. All samples were checked for and did not exhibit charging, which was verified by X-ray power dependence measurements. For all samples measured, Ni was present; however, the amount of Ni was nitinol batch dependent and does not influence our XPS/UPS conclusions to the best of our knowledge. Previous XPS studies on analogous samples showed Ni present at the surface, but decreased rapidly below the surface where a Ni free oxide zone was observed.⁴⁰ Samples that were oxidized for 120 min (100 nm) showed analogous electrochemistry, however

were more prone to surface fissuring (Figure S4). For strain measurements, samples were loaded into an MTI/Fullam SEMTester equipped with a 450 N capacity load cell and controlled using MTESTQuattro control software. Samples were strained at a rate of 2 mm/min. Electrochemical measurements were controlled by a CH Instruments 600D potentiostat using a custom-built single compartment cell with a Ag/AgCl reference electrode and platinum counter (Figure S1). Phosphate buffer (0.1 M) was used as the electrolyte. Impedance measurements were carried out at frequencies ranging from 100 Hz to 2 GHz with an amplitude of 10 mV at a potential where no faradaic process is observed (0 V vs. Ag/AgCl). MS measurements were taken at 10, 100, and 1000 Hz with an amplitude of 10 mV. For a typical experiment, the cell is loosely assembled around the NiTi sample, and then the sample is pre-strained to 5 N (taken as 0% strain). The cell is then tightened onto the sample to create a solution tight cell for electrochemical measurements. To strain the working NiTi electrode, the electrolyte is drained and the cell loosened so that the sample can move freely, and then the strain is adjusted under software control. The cell is then re-aligned, gently tightened back onto the sample, and the electrolyte is replaced for further measurements. This procedure is repeated at each strain value.

Conducting Atomic Force Microscopy (CAFM): These measurements were made with a Digital Instruments, Nanoscope V Atomic Force Microscope System by Veeco. The CAFM is housed in an acoustic box and seated on a vibration isolation table. Current vs. voltage plots were recorded using contact mode AFM tips (DDESP-V2 by Bruker). Methyl viologen dichloride (MV) was purchased from Sigma-Adrich, and $\text{Ru}(\text{NH}_3)_6\text{Cl}_3$ was purchased from Polysciences. All chemicals were used as received. For XPS/UPS and CAFM experiments, a sample requires being removed from the tensile tester under strain. Therefore, the sample is strained using the tensile

tester and then a static strain holder (Figure S2) is attached and securely clamped to the sample before removal from the tensile tester.

Associated Content.

Schematics of the electrochemical cell and static strain holders, CVs of electrochemical standards taken after stretch experiments at a gold electrode, table of EIS fitting parameters, SEM images of polished, oxidized and strained samples, MS and series capacitance of samples at 10, 100, and 1000 Hz, as well as high resolution XPS spectra of samples can be found in the supporting information.

Acknowledgements.

This work was funded by the U.S. Department of Energy, Office of Science, Basic Energy Science, Division of Chemical Sciences, Geosciences and Biosciences, under Contract No. DE-AC36-08GO28308 to NREL.

References

1. Elastic Strain Engineering. *MRS Bull.* **2014**, 39, (02).
2. Darensbourg, M. Y.; Lyon, E. J.; Zhao, X.; Georgakaki, I. P., The organometallic active site of [Fe]hydrogenase: Models and entatic states. *Proc. Natl. Acad. Sci. U.S.A.* **2003**, 100, (7), 3683-3688.
3. Ringe, D.; Petsko, G. A., How Enzymes Work. *Science* **2008**, 320, (5882), 1428-1429.
4. Vallee, B. L.; Williams, R. J., Metalloenzymes: the entatic nature of their active sites. *Proc. Natl. Acad. Sci. U.S.A.* **1968**, 59, (2), 498-505.
5. Bissett, M. A.; Konabe, S.; Okada, S.; Tsuji, M.; Ago, H., Enhanced Chemical Reactivity of Graphene Induced by Mechanical Strain. *ACS Nano* **2013**, 7, (11), 10335-10343.

6. Reske, R.; Duca, M.; Oezaslan, M.; Schouten, K. J. P.; Koper, M. T. M.; Strasser, P., Controlling Catalytic Selectivities during CO₂ Electroreduction on Thin Cu Metal Overlayers. *J. Phys. Chem. Lett.* **2013**, 4, (15), 2410-2413.
7. Svedruzic, D.; Gregg, B. A., Mechano-Electrochemistry and Fuel-Forming Mechano-Electrocatalysis on Spring Electrodes. *J. Phys. Chem. C* **2014**, 118, (33), 19246-19251.
8. Du, M.; Cui, L.; Cao, Y.; Bard, A. J., Mechanoelectrochemical Catalysis of the Effect of Elastic Strain on a Platinum Nanofilm for the ORR Exerted by a Shape Memory Alloy Substrate. *J. Am. Chem. Soc.* **2015**, 137, (23), 7397-7403.
9. Muralidharan, N.; Carter, R.; Oakes, L.; Cohn, A. P.; Pint, C. L., Strain Engineering to Modify the Electrochemistry of Energy Storage Electrodes. *Sci. Rep.* **2016**, 6, 27542.
10. Mavrikakis, M.; Hammer, B.; Nørskov, J. K., Effect of Strain on the Reactivity of Metal Surfaces. *Phys. Rev. Lett.* **1998**, 81, (13), 2819-2822.
11. Sun, Y.; Thompson, S. E.; Nishida, T., Physics of strain effects in semiconductors and metal-oxide-semiconductor field-effect transistors. *J. Appl. Phys.* **2007**, 101, (10), 104503.
12. Niquet, Y.-M.; Delerue, C.; Krzeminski, C., Effects of Strain on the Carrier Mobility in Silicon Nanowires. *Nano Letters* **2012**, 12, (7), 3545-3550.
13. Asai, H.; Oe, K., Energy band-gap shift with elastic strain in Ga_xIn_{1-x}P epitaxial layers on (001) GaAs substrates. *J. Appl. Phys.* **1983**, 54, (4), 2052-2056.
14. Chu, M.; Sun, Y.; Aghoram, U.; Thompson, S. E., Strain: A Solution for Higher Carrier Mobility in Nanoscale MOSFETs. *Annu. Rev. Mater. Res.* **2009**, 39, (1), 203-229.
15. Huo, Y.; Lin, H.; Chen, R.; Makarova, M.; Rong, Y.; Li, M.; Kamins, T. I.; Vuckovic, J.; Harris, J. S., Strong enhancement of direct transition photoluminescence with highly tensile-strained Ge grown by molecular beam epitaxy. *Appl. Phys. Lett.* **2011**, 98, (1), 011111.
16. Greil, J.; Lugstein, A.; Zeiner, C.; Strasser, G.; Bertagnolli, E., Tuning the Electro-optical Properties of Germanium Nanowires by Tensile Strain. *Nano Letters* **2012**, 12, (12), 6230-6234.
17. Walsh, A.; Ahn, K.-S.; Shet, S.; Huda, M. N.; Deutsch, T. G.; Wang, H.; Turner, J. A.; Wei, S.-H.; Yan, Y.; Al-Jassim, M. M., Ternary cobalt spinel oxides for solar driven hydrogen production: Theory and experiment. *Energy Environ. Sci.* **2009**, 2, (7), 774-782.
18. Abdi, F. F.; Han, L.; Smets, A. H. M.; Zeman, M.; Dam, B.; van de Krol, R., Efficient solar water splitting by enhanced charge separation in a bismuth vanadate-silicon tandem photoelectrode. *Nat. Commun.* **2013**, 4.
19. Kim, T. W.; Choi, K.-S., Nanoporous BiVO₄ Photoanodes with Dual-Layer Oxygen Evolution Catalysts for Solar Water Splitting. *Science* **2014**, 343, (6174), 990-994.

20. Guo, W.; Chemelewski, W. D.; Mabayoje, O.; Xiao, P.; Zhang, Y.; Mullins, C. B., Synthesis and Characterization of CuV₂O₆ and Cu₂V₂O₇: Two Photoanode Candidates for Photoelectrochemical Water Oxidation. *J. Phys. Chem. C* **2015**, 119, (49), 27220-27227.
21. Lee, K.; Ruddy, D. A.; Dukovic, G.; Neale, N. R., Synthesis, optical, and photocatalytic properties of cobalt mixed-metal spinel oxides Co(Al_{1-x}Ga_x)₂O₄. *J. Mater. Chem. A* **2015**, 3, (15), 8115-8122.
22. Seabold, J. A.; Neale, N. R., All First Row Transition Metal Oxide Photoanode for Water Splitting Based on Cu₃V₂O₈. *Chem. Mater.* **2015**, 27, (3), 1005-1013.
23. Zhou, L.; Yan, Q.; Shinde, A.; Guevarra, D.; Newhouse, P. F.; Becerra-Stasiewicz, N.; Chatman, S. M.; Haber, J. A.; Neaton, J. B.; Gregoire, J. M., High Throughput Discovery of Solar Fuels Photoanodes in the CuO–V₂O₅ System. *Adv. Energy Mater.* **2015**, 5, (22), 1500968-n/a.
24. Trotochaud, L.; Ranney, J. K.; Williams, K. N.; Boettcher, S. W., Solution-Cast Metal Oxide Thin Film Electrocatalysts for Oxygen Evolution. *J. Am. Chem. Soc.* **2012**, 134, (41), 17253-17261.
25. Hu, S.; Shaner, M. R.; Beardslee, J. A.; Lichterman, M.; Brunschwig, B. S.; Lewis, N. S., Amorphous TiO₂ coatings stabilize Si, GaAs, and GaP photoanodes for efficient water oxidation. *Science* **2014**, 344, (6187), 1005-1009.
26. Yang, Y.; Gu, J.; Young, J. L.; Miller, E. M.; Turner, J. A.; Neale, N. R.; Beard, M. C., Semiconductor interfacial carrier dynamics via photoinduced electric fields. *Science* **2015**, 350, (6264), 1061-1065.
27. Gu, J.; Yan, Y.; Young, J. L.; Steirer, K. X.; Neale, N. R.; Turner, J. A., Water reduction by a p-GaInP₂ photoelectrode stabilized by an amorphous TiO₂ coating and a molecular cobalt catalyst. *Nat. Mater.* **2016**, 15, (4), 456-460.
28. Jia, L.; Shu, D.-J.; Wang, M., Tuning the Area Percentage of Reactive Surface of TiO₂ by Strain Engineering. *Phys. Rev. Lett.* **2012**, 109, (15), 156104.
29. Yin, W.-J.; Chen, S.; Yang, J.-H.; Gong, X.-G.; Yan, Y.; Wei, S.-H., Effective band gap narrowing of anatase TiO₂ by strain along a soft crystal direction. *Appl. Phys. Lett.* **2010**, 96, (22), 221901.
30. Shu, D.-J.; Ge, S.-T.; Wang, M.; Ming, N.-B., Interplay between External Strain and Oxygen Vacancies on a Rutile TiO₂ (110) Surface. *Phys. Rev. Lett.* **2008**, 101, (11), 116102.
31. Pan, X.; Yang, M.-Q.; Fu, X.; Zhang, N.; Xu, Y.-J., Defective TiO₂ with oxygen vacancies: synthesis, properties and photocatalytic applications. *Nanoscale* **2013**, 5, (9), 3601-3614.

32. Heckel, W.; Wehlau, M.; Maisel, S. B.; Frauenheim, T.; Knaup, J. M.; Müller, S., How the aggregation of oxygen vacancies in rutile-based TiO₂- δ phases causes memristive behavior. *Phys. Rev. B* **2015**, 92, (21), 214104.
33. Amato, M.; Rurali, R., Shell-Thickness Controlled Semiconductor–Metal Transition in Si–SiC Core–Shell Nanowires. *Nano Letters* **2015**, 15, (5), 3425-3430.
34. Johari, P.; Shenoy, V. B., Tuning the Electronic Properties of Semiconducting Transition Metal Dichalcogenides by Applying Mechanical Strains. *ACS Nano* **2012**, 6, (6), 5449-5456.
35. Scalise, E.; Houssa, M.; Pourtois, G.; Afanas'ev, V.; Stesmans, A., Strain-induced semiconductor to metal transition in the two-dimensional honeycomb structure of MoS₂. *Nano Res.* **2011**, 5, (1), 43-48.
36. Song, S.; Keum, D. H.; Cho, S.; Perello, D.; Kim, Y.; Lee, Y. H., Room Temperature Semiconductor–Metal Transition of MoTe₂ Thin Films Engineered by Strain. *Nano Letters* **2016**, 16, (1), 188-193.
37. Molaei, R.; Bayati, R.; Wu, F.; Narayan, J., A microstructural approach toward the effect of thickness on semiconductor-to-metal transition characteristics of VO₂ epilayers. *J. Appl. Phys.* **2014**, 115, (16), 164311.
38. Kim, H.; Charipar, N.; Osofsky, M.; Qadri, S. B.; Piqué, A., Optimization of the semiconductor-metal transition in VO₂ epitaxial thin films as a function of oxygen growth pressure. *Appl. Phys. Lett.* **2014**, 104, (8), 081913.
39. Mohd Jani, J.; Leary, M.; Subic, A.; Gibson, M. A., A review of shape memory alloy research, applications and opportunities. *Mater. Des.* **2014**, 56, 1078-1113.
40. Firstov, G. S.; Vitchev, R. G.; Kumar, H.; Blanpain, B.; Van Humbeeck, J., Surface oxidation of NiTi shape memory alloy. *Biomaterials* **2002**, 23, (24), 4863-4871.
41. Metikoš-Huković, M.; Katić, J.; Milošev, I., Kinetics of passivity of NiTi in an acidic solution and the spectroscopic characterization of passive films. *J. Solid State Electrochem.* **2012**, 16, (7), 2503-2513.
42. Abidi, I. H.; Cagang, A. A.; Tyagi, A.; Riaz, M. A.; Wu, R.; Sun, Q.; Luo, Z., Oxidized nitinol substrate for interference enhanced Raman scattering of monolayer graphene. *RSC Adv.* **2016**, 6, (9), 7093-7100.
43. Scheuermann, A. G.; Prange, J. D.; Gunji, M.; Chidsey, C. E. D.; McIntyre, P. C., Effects of catalyst material and atomic layer deposited TiO₂ oxide thickness on the water oxidation performance of metal-insulator-silicon anodes. *Energy Environ. Sci.* **2013**, 6, (8), 2487-2496.
44. Leng, W. H.; Zhang, Z.; Zhang, J. Q.; Cao, C. N., Investigation of the Kinetics of a TiO₂ Photoelectrocatalytic Reaction Involving Charge Transfer and Recombination through Surface States by Electrochemical Impedance Spectroscopy. *J. Phys. Chem. B* **2005**, 109, (31), 15008-15023.

45. Connor, P. A.; McQuillan, A. J., Phosphate Adsorption onto TiO₂ from Aqueous Solutions: An in Situ Internal Reflection Infrared Spectroscopic Study. *Langmuir* **1999**, 15, (8), 2916-2921.
46. Hirschorn, B.; Orazem, M. E.; Tribollet, B.; Vivier, V.; Frateur, I.; Musiani, M., Determination of effective capacitance and film thickness from constant-phase-element parameters. *Electrochim. Acta* **2010**, 55, (21), 6218-6227.
47. Kavan, L.; Grätzel, M.; Gilbert, S. E.; Klemenz, C.; Scheel, H. J., Electrochemical and Photoelectrochemical Investigation of Single-Crystal Anatase. *J. Am. Chem. Soc.* **1996**, 118, (28), 6716-6723.
48. Morrison, S. R., *Electrochemistry at Semiconductor and Oxidized Metal Electrodes*. Plenum Press: New York, NY, 1980.
49. Li, Z.; Potapenko, D. V.; Osgood, R. M., Controlling Surface Reactions with Nanopatterned Surface Elastic Strain. *ACS Nano* **2015**, 9, (1), 82-87.
50. Wang, Z.-W.; Shu, D.-J.; Wang, M.; Ming, N.-B., Strain effect on diffusion properties of oxygen vacancies in bulk and subsurface of rutile TiO₂. *Surf. Sci.* **2012**, 606, (3-4), 186-191.
51. Perkins, C. L.; Hasoon, F. S., Surfactant-assisted growth of CdS thin films for photovoltaic applications. *J. Vac. Sci. Technol. A* **2006**, 24, (3), 497-504.

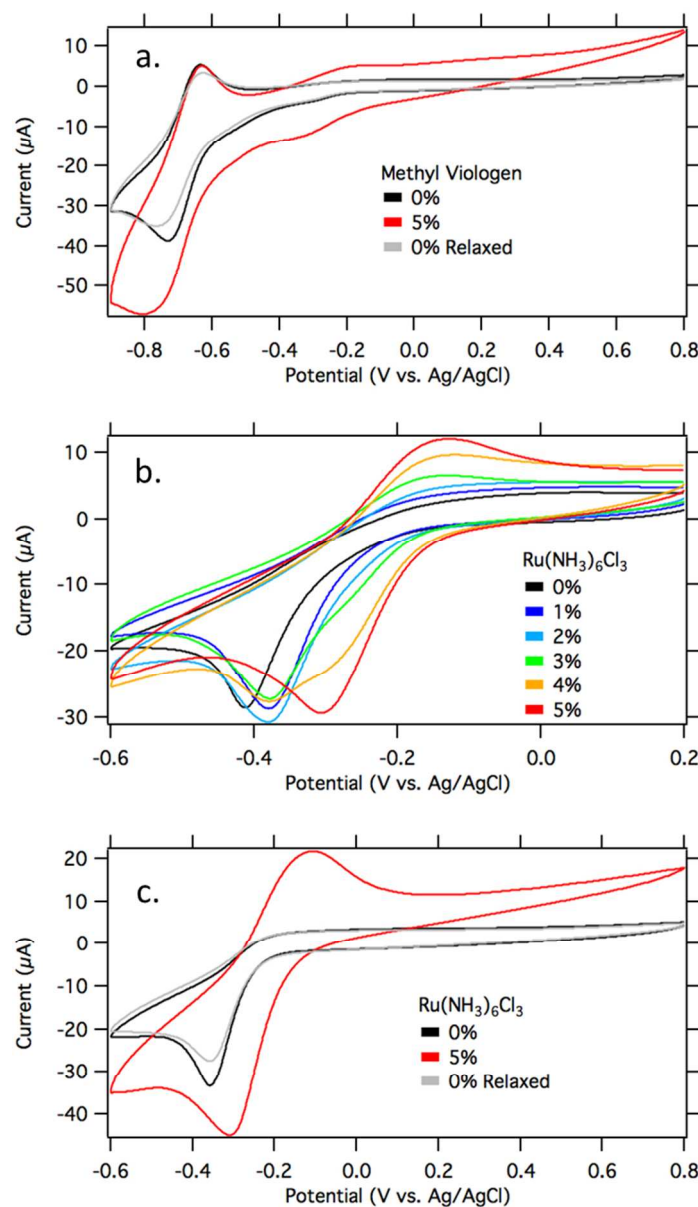


Figure 1. a) Cyclic voltammograms (CVs) of 1 mM methyl viologen at 0%, 5%, and relaxed to 0% strain of a 50 nm TiO_2 film. b) 1 mM ruthenium hexamine at 0% – 5% applied external strain at 1% strain intervals c) CVs of 1 mM ruthenium hexamine in at 0%, 5%, and relaxed back to 0% external strain. All scans were taken in 0.1 M phosphate buffer (pH 7) on a 50 nm TiO_2 film at 50 mV/s with Ag/AgCl reference and Pt counter electrodes.

198x330mm (96 x 96 DPI)

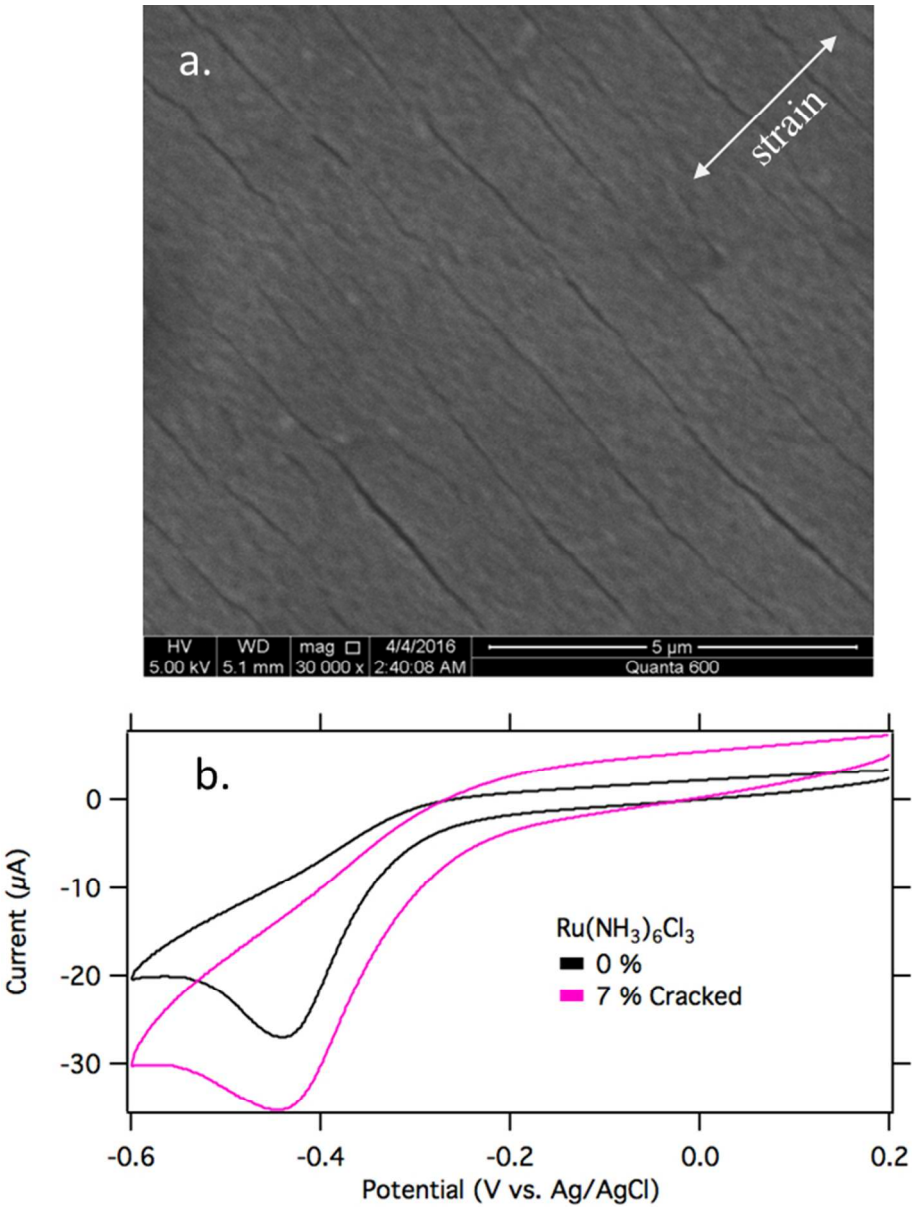


Figure 2. a) SEM image of the cracked TiO₂ film under 7% strain showing the formation of fissures forming perpendicular to the direction of strain. b) CVs of 1 mM ruthenium hexamine at a intentionally cracked 50 nm TiO₂ film at 0% and 7% external applied strain

198x249mm (96 x 96 DPI)

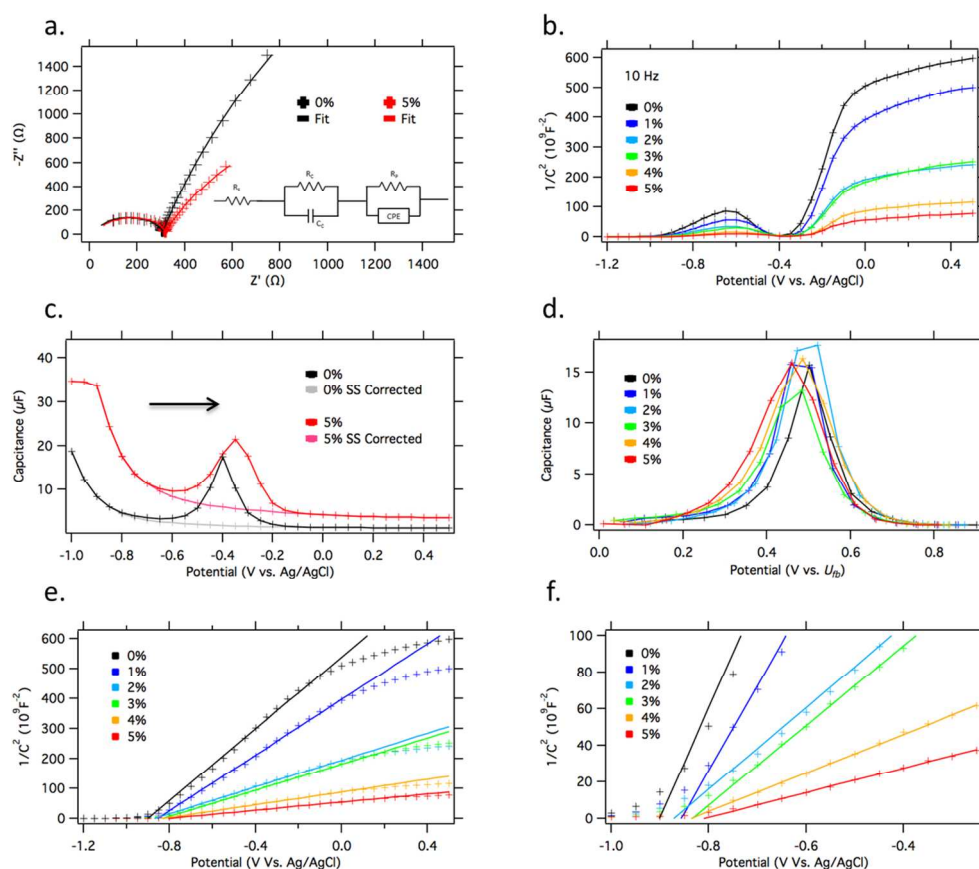


Figure 3. a) Nyquist plot and circuit model for 50 nm TiO_2 films (0 and 5% strain) in 1 mM ruthenium hexamine in 0.1 M phosphate buffer taken at 0.00 V where no redox processes take place. Data is taken from 100 Hz to 2 MHz. b) Mott-Schottky (MS) plot of strained TiO_2 films taken at 10 Hz c) Series capacitance of 0% and 5% strain before and after ("corrected") surface state (SS) deconvolution d) SS capacitance plotted vs. U_{fb} used for deconvolution of MS plot e) SS deconvoluted MS plot and fits (solid lines) and f) expanded region of the MS plot near the U_{fb}

335x292mm (96 x 96 DPI)

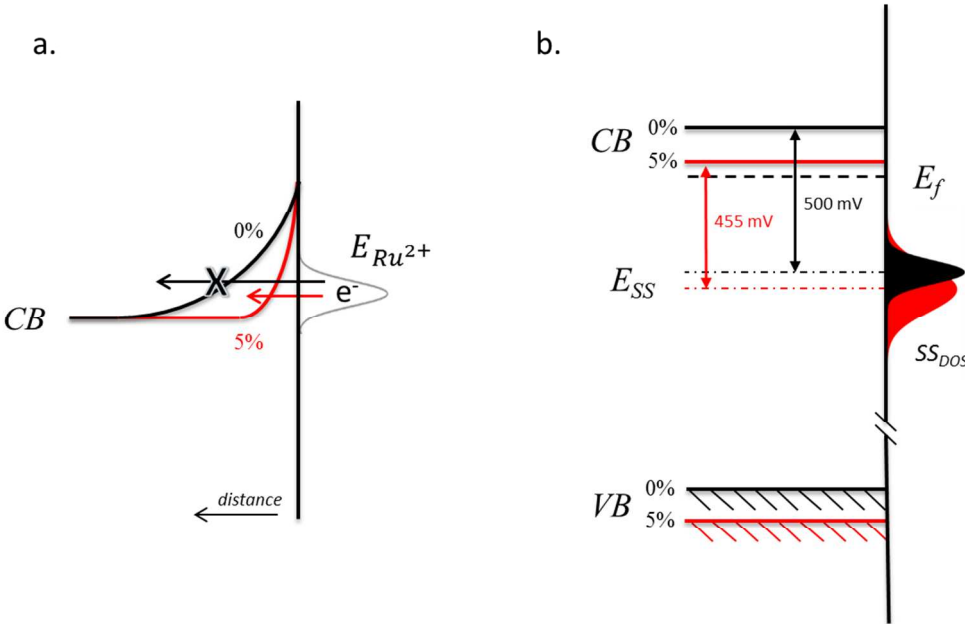


Figure 4. a) Proposed band diagram showing the effect of strain on the depletion width and resulting electron tunneling from the reduced species to the conduction band and b) energy diagram under flat band conditions showing the effect of strain on the surface state energy level distribution and the shift of the conduction band relative to the Fermi level, E_f .

296x186mm (96 x 96 DPI)

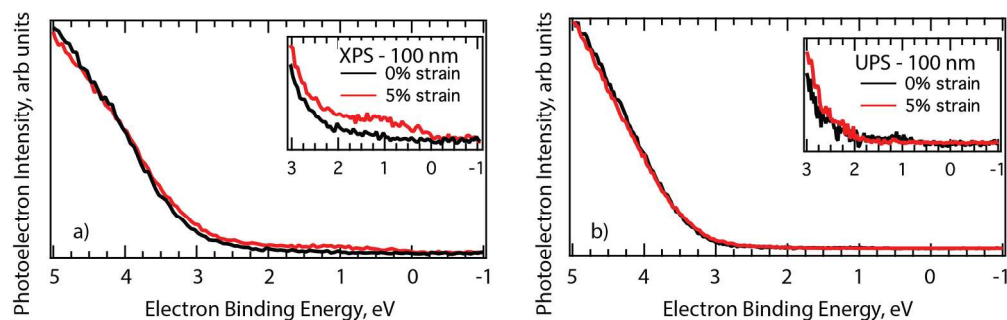


Figure 5. a) XPS and b) UPS valence band region of TiO₂/NiTi under 0% (black trace) and 5% (red trace) strain. The photoelectron intensity at $E_F = 0$ eV is present in the XPS and not UPS, which is emphasized in the insets.

193x59mm (300 x 300 DPI)

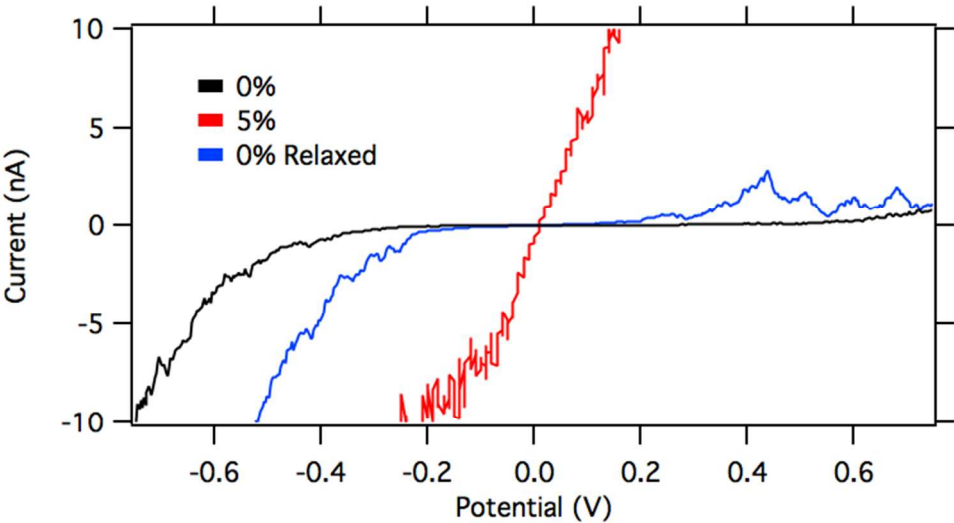


Figure 6. Current-voltage curves obtained from CAFM measurements of 50 nm TiO₂ films at 0%, 5% and then relaxed to 0% strain.

140x73mm (143 x 143 DPI)